

Article

X-ray Photospectroscopy and Electronic Studies of Reactor Parameters on Photocatalytic Hydrogenation of Carbon Dioxide by Defect-Laden Indium Oxide Hydroxide Nanorods

Joel Y. Y. Loh ¹  and Nazir P. Kherani ^{1,2,*}

¹ Department of Electrical and Computing Engineering, University of Toronto, Toronto, ON M5S 3G4, Canada; joel.loh@mail.utoronto.ca

² Department of Material Science and Engineering, University of Toronto, Toronto, ON M5S 3E4, Canada

* Correspondence: kherani@ecf.utoronto.ca; Tel.: +1-416-946-7372

Academic Editors: Marcelo I. Guzman and German Mills

Received: 31 August 2019; Accepted: 9 October 2019; Published: 23 October 2019



Abstract: In the study reported herein, glovebox-protected X-ray photoelectron spectroscopy (XPS) and in situ Hall charge carrier measurements provide new insights into the surface physical chemistry of gaseous H₂, CO₂, and H₂+CO₂ combined with nanostructured In₂O_(3-x)(OH)_y nanorods, which ensue under photochemical and thermochemical operating conditions. Heterolytic dissociation of H₂ in H₂-only atmosphere appears to occur mainly under dark and ambient temperature conditions, while the greatest amount of OH shoulder expansion in H₂+CO₂ atmosphere appears to mainly occur under photoilluminated conditions. These results correlate with those of the Hall measurements, which show that the prevalence of homolytic over heterolytic dissociation at increasing temperatures leads to a steeper rate of increase in carrier concentrations; and that H₂ adsorption is more prevalent than CO₂ in H₂+CO₂ photoillumination conditions.

Keywords: indium oxide; reverse water gas shift; X-ray photospectroscopy; hall mobility

1. Introduction

Photocatalysts are useful tools in the reduction of CO₂ under solar radiation to generate sustainable fuels [1–3]. The thermal dehydroxylation of In(OH)₃ at 500 °C yields the cubic bixbyite In₂O₃ polymorph, the crystal structure of which is based on fluorite, with 25% of the oxide ions missing from the lattice. By controlling the thermal profile used for the dehydroxylation of the In(OH)₃ precursor, a partially dehydroxylated indium oxide hydroxide is obtained, in which the bixbyite structure is retained [4–8]. By quantifying the amount of water eliminated from the lattice of In(OH)₃ by thermal gravimetric analysis, the stoichiometry of the oxide and hydroxide groups in the obtained material can be established according to the balanced reaction equation, with the following intermediate stoichiometric composition: 2In(OH)₃ → In₂O_{2x}(OH)_(6-x) + 2xH₂O → In₂O₃ + 3H₂O (~300 °C). The intermediate indium oxide hydroxide product at 250 °C In₂O_{2x}(OH)_(6-4x), denoted In₂O_(3-x)(OH)_y, thus, contains hydroxide groups and coordinately unsaturated indium sites, denoted InOH••In. These sites behave as a Lewis base and a Lewis acid individually, but when coupled together can be viewed as a metastable surface frustrated Lewis pair (SFLP) site [9,10]. Oxygen vacancies also exist in the lattice of In₂O_(3-x)(OH)_y, which serve to increase the Lewis acidity of adjacent indium sites. These defects, both coupled and uncoupled, all play pivotal roles in catalyzing the light-assisted reverse water gas shift (RWGS) reaction [11]: CO₂ + H₂ → CO + H₂O. Depending on the ratio of H₂ to CO₂ pressure fraction, the selectivity of the RWGS can range from CH₄ to CO or CH₃OH. The main product of the 1:1 pressure

ratio of H₂:CO₂ on the In₂O_(3-x)(OH)_y catalyst is CO, with a typical yield range of 20–120 ppm/g.cat over a reactor temperature of 100–200 °C, with minor CH₄ yield.

For amplification, the first step in the RWGS catalytic cycle (CO₂ + H₂ → CO + H₂O) is purported to involve heterolysis of H₂ on the SFLP to form InOH₂••InH, comprised of a proton bound to the hydroxide Lewis base site and a negatively charged hydride to the coordinately unsaturated Lewis acid indium site. The rationale for the heterolytic splitting of H₂ is due to the strong charge polarization effect of the indium site and OH site [12–14]. In general, various polar metal oxides, such as MgO and CeO₂ [15–17] were shown to have strong polarization between the metal and oxide sites, which would heterolytically split H₂; in In₂O_(3-x)(OH)_y the polarization is induced by the presence of the oxygen vacancy between the indium and OH sites. In the rest of the cycle, an intermediate formate carbonate species is generated on the InOH₂••InH supersite, before decomposing into CO and H₂O from the C–OH₂In end and the O–HIn end. In the work described herein, quasi-operando X-ray photoelectron spectroscopy (XPS) probes the interaction of H₂, CO₂, and H₂+CO₂ with the surface of pristine nanostructured In₂O_(3-x)(OH)_y. The difference between an ex situ XPS measurement and the following study is that the reactors with the samples contained within were directly transferred into the glovebox after the various gas treatments, and the samples were transferred to the XPS within the argon-filled glovebox. Hence, the surface condition reflects that of the stable chemisorbed species after reactor treatments. These results provide a deeper understanding of the chemistry in the ground and excited states relevant to the RWGS reaction. We also conducted in situ Hall carrier property measurements under the various gas reactant atmospheres in dark and photoillumination conditions, which allowed us to associate the chemisorption of the reactants to the electronic properties of the In₂O_(3-x)(OH)_y nanorods.

2. Results and Discussion

The CO production rate from the reverse water gas shift reaction on In₂O_(3-x)(OH)_y nanorods shows a significantly greater enhancement under white light photoillumination of 140 mW/cm² than under dark conditions, with the increase in CO rate diminishing with higher temperatures. The maximum rate under white light and reactor temperature of 210 °C is 50.2 μmol/g.cat/hour, with a pseudo activation energy of 10.9 kJ/mol/K, which is smaller by a factor of 0.46 than the activation energy under dark conditions. The XPS O1s core-level binding energies of In₂O_(3-x)(OH)_y nanorods in a vacuum can be resolved into four peaks (limited to a maximum of 1.4 eV FWHM), assigned to lattice oxide around ~529.5 eV, oxygen vacancy ~530.5 eV, hydroxide ~532 eV, and protonated OH groups at ~532.5 eV (Figure 1b). The line widths of these O1s peaks are often broad and asymmetric because of multiple site occupancies of oxide lattice O_{lattice} (40% of total species), oxygen vacancies O_{vac} (21%), and hydroxide OH type species (39%) on the surface of In₂O_(3-x)(OH)_y. The effective positive charge of the proton bonded to the oxide site of the hydroxide causes the O1s ionization potentials to shift to higher energy than the lattice oxide, while the protonated OH species (H⁺OH) (14% of total species) arising from ambient moisture during synthesis preparation [18,19] causes a positive shift for some of the OH groups, which all result in a broad OH shoulder. In addition, the presence of an oxygen vacancy in the oxide coordination sphere of indium enhances binding of the remaining oxides to the indium, which is manifest as a shift to higher energy of the O1s ionization potentials. We note that all In3d peaks were normalized between the various conditions, and the same normalization factor applied towards the O1s and C1s spectra. The corresponding In3d XPS results for nanostructured In₂O_(3-x)OH_y are shown in (Figure 1c). The In3d^{3/2} spin orbit component is found to have an ionization potential around 444 eV. Its line width contains contributions from In–OH and In–O species, of which the 41% ratio of OH-type species over the total is similar to that of the O1s spectrum.

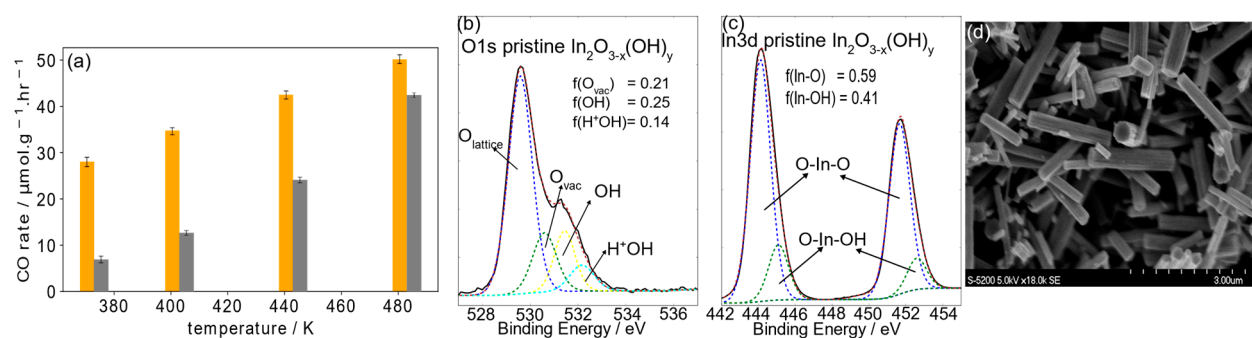


Figure 1. (a) The CO production rate with the $\text{In}_2\text{O}_{(3-x)}(\text{OH})_y$ catalyst under white light at 1:1 pressure ratio of $\text{H}_2:\text{CO}_2$ gas atmosphere, and under dark conditions with increasing reactor temperatures. (b,c) The O1s and In3d XPS spectrum of $\text{In}_2\text{O}_{(3-x)}(\text{OH})_y$ nanorods as prepared. (d) SEM topographical image of $\text{In}_2\text{O}_{(3-x)}(\text{OH})_y$ nanorods.

On exposure of $\text{In}_2\text{O}_{(3-x)}(\text{OH})_y$ nanorods to H_2 at under dark and ambient room temperature (dark ambient) conditions a dramatic increase in the intensity and shift to high energy of approximately 0.5 eV occurs for the O1s binding energy of the hydroxide (Figure 2). This observation flags the dissociation of H_2 on the surface of $\text{In}_2\text{O}_{(3-x)}(\text{OH})_y$. Noticeably, the fraction of O_{vac} remains similar for all conditions under H_2 , indicating that the new hydroxide formation associated with ~ 532.2 eV is mostly hydrogen adatoms on lattice oxide sites to form bridging OH groups. Concomitantly the $\text{In}3d^{3/2}$ peak undergoes a notable shift to lower energy implying the indium is experiencing a lower effective nuclear charge (Figure 2b). This behavior arises from a coordinately unsaturated Lewis acidic surface indium site bonded to a highly nucleophilic hydride formed by heterolysis of H_2 on a SFLP site, which must dominate the opposing effect of protonation (Figure 2d). In addition, homolysis of H_2 on hydroxide surface sites adjacent the oxygen vacancy sites, protonates these OH groups. The associated injection of charge-balancing electrons into defect indium sites cause the $\text{In}3d^{3/2}$ peak to shift to lower energy, providing it overrides the countering effect of protonation. With H_2 exposure under photoillumination, the intensity of the OH shoulder shrinks below its dark ambient value. Since the OH shoulder also experiences a small binding energy decrease from dark ambient to phototreatment, this indicates that H^+ adatoms on OH groups are removed, and less so for H^+ adatoms on lattice oxide sites. Heating at 150 °C causes further shrinkage of the intensity of this OH shoulder. The OH shoulder binding energy is similar to that of the H_2 dark ambient condition, indicating that more H adatoms on lattice oxides are removed and less so for H adatoms bound on OH groups. These observations signal the photochemical and thermochemical induced loss of H_2O from protonated hydroxide and indium hydride sites which indicates that indium hydride sites are photo and thermally unstable. Additionally, with introduction of H_2 there is a diminishment of the intensity of C1s peaks indicating removal of C–C surface contaminants on the $\text{In}_2\text{O}_{(3-x)}\text{OH}_y$ nanorods (Figure 2e). Further information on the deconvolution of the O1s spectra are shown in the supplementary section.

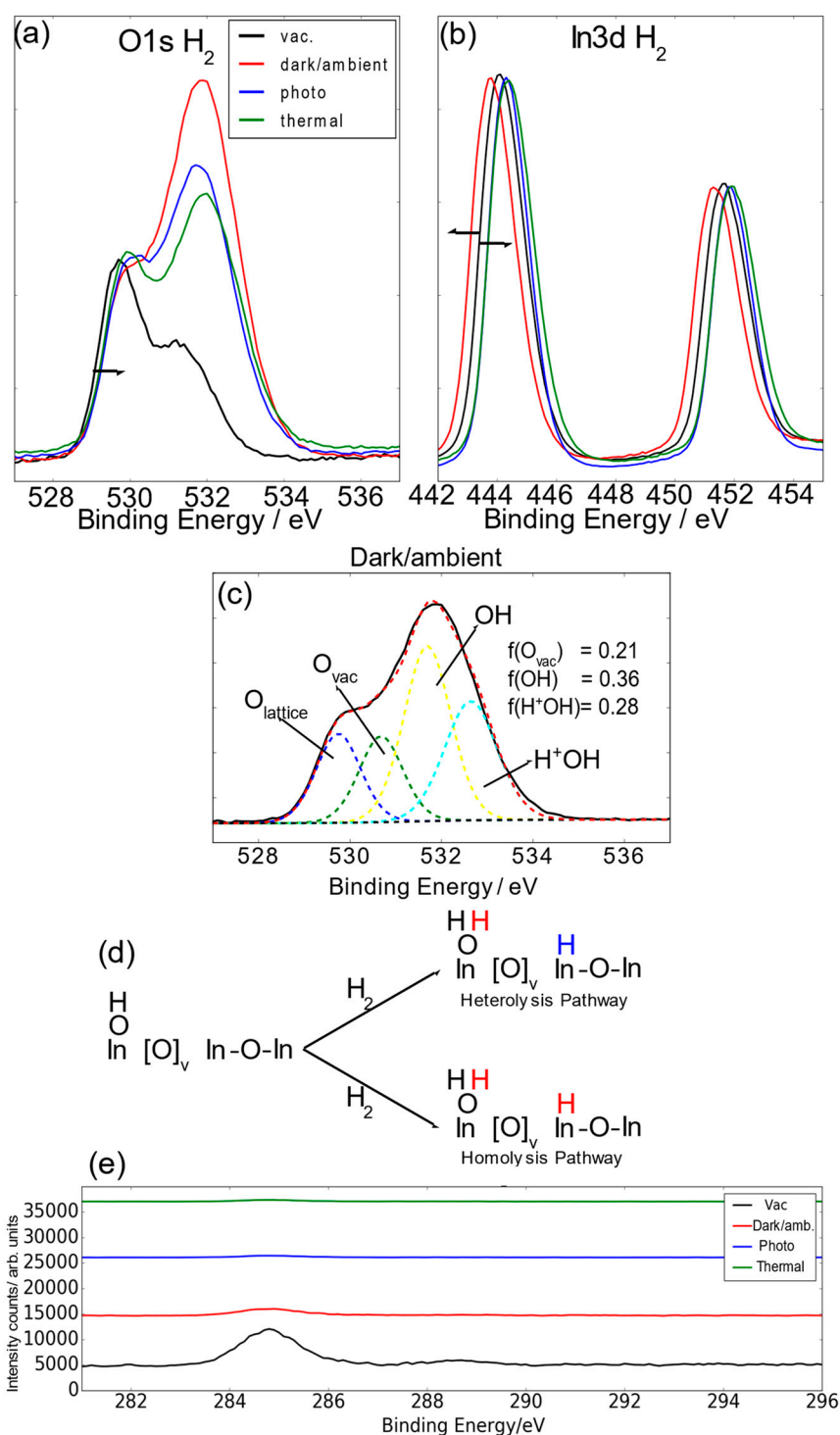


Figure 2. (a,b) The O1s and In3d X-ray photoelectron spectroscopy (XPS) spectra of $\text{In}_2\text{O}_{(3-x)}(\text{OH})_y$ nanorods in H_2 under various reactor conditions in comparison with the pristine surface shown in Figure 1. (c) The XPS deconvolution of the O1s spectrum under H_2 dark ambient conditions into various oxygen species. (d) Heterolysis and homolysis dissociation of H_2 molecules over a surface frustrated Lewis acid–base pair site. (e) C1s spectra of $\text{In}_2\text{O}_{(3-x)}(\text{OH})_y$ under H_2 in various conditions.

The XPS study of O1s, In3d, and C1s surface species arising from the interaction of the acidic CO_2 gas probe under dark ambient conditions on pristine, nanostructured $\text{In}_2\text{O}_{(3-x)}(\text{OH})_y$ is rich in detail (Figure 3). In the C1s XPS, the growth of new peaks in the region of 285–288 eV signals the adsorption or reaction of CO_2 with oxygen vacancy, hydroxide, and coordinately unsaturated

indium surface sites. Monodentate configurations are more favorable on surfaces with high basicity and bidentate, or tridentate configurations on surfaces with low basicity. It has been shown that on In_2O_3 surfaces, tridentate and bidentate configurations are favourable [12]. For example, two types of tridentate configurations are energetically favorable, where in one case, the carbonate bridges two In-O-In chains to form a cross-wise configuration with an absorption energy of -1.14 eV; in the other case, a tridentate configuration, where the CO_2 is in the same plane as In-O-In , the absorption energy is -1.25 eV. A conventional bidentate configuration of carbonate has an absorption energy of -0.70 eV. The significant amount of C–O and O=C signals indicate that bidentate and tridentate carbonate configurations are dominant, while the increased O=C–O/O=C–OH signal indicates bicarbonate products from CO_2 reactions with OH groups. This model receives support from the corresponding O1s XPS, where adsorption or reaction of CO_2 in general with $\text{In}_2\text{O}_{(3-x)}\text{OH}_y$ increases the effective nuclear charge of the oxide, seen as a small shift of the O1s to higher energy. The hydroxide shoulder around 532 eV increases in height and widens in dark ambient CO_2 atmosphere, indicating highly positively charged oxide species as a result of the exposure of carbonate species to the O1s spectrum, with C–O species in the range of 531.5–532.0 eV, C=O in the range of 532.0–533.0 eV, and O=C–O species from 533.3–533.6 eV. The effect of light removes the higher binding energy component in the O1s spectrum, indicating surface bicarbonate fragmenting to CO_2 and H_2O . The remaining bidentate and tridentate carbonates induce a higher OH shoulder than that of the vacuum state. The removal of bidentate carbonates to leave behind carbonate configurations with dominant C–O bonds under thermal treatment narrows the OH shoulder and shifts the $\text{O}_{\text{Lattice}}$ subpeak to a higher binding energy, which indicates that either tridentate carbonates or oxygen vacancies may have been filled by carbon dioxide to form species with C–O bonds. This indicates that only such carbonate species persist under thermal treatment.

On exposure of nanostructured $\text{In}_2\text{O}_{(3-x)}\text{OH}_y$ to both H_2 and CO_2 under ambient temperature, thermal, and photo conditions, the O1s XPS spectrum shows a substantial increase in the intensity of the hydroxide shoulder, with a concurrent shift to higher energy of the latter oxide peak, while the In3d XPS spectra show a similarly small shift. The C1s XPS spectra reveal the presence of C–O-containing species generated photochemically from the reaction of H_2 and CO_2 to generate a C1s spectra similar to that of CO_2 -only thermal conditions (Figure 4). There is also an increased C1s signal at ~ 288 – 289 eV, indicating C=O and O–C=O species. Since the O1s ionization potential shift is greater for photo than for dark ambient conditions, this implies that part of the OH shoulder height increase is due to increased H_2 dissociation on both OH and $\text{O}_{\text{Lattice}}$ sites, and part of it is due to increased carbonate formation. The results, thus, suggest that the surface is highly active under photo conditions. H_2 + CO_2 mix to form a basic surface that enables adsorption of CO_2 molecules as bidentate and tridentate species, since C–O and O–C=O bonds seem to be the most stable bond formations under photo conditions. This can be linked to the photoexcited valence band holes and conduction band electrons into the hydroxide Lewis base defect near the conduction band edge, and indium Lewis acid defects near the valence band edge. The trapped electron and hole enhance the Lewis acidity and basicity of any indium hydride and protonated hydroxide group in the excited state, compared to the ground state [20,21]. However, one difference between the H_2 and H_2 + CO_2 atmosphere is the straddle between the $\text{O}_{\text{lattice}}$ peak and OH species-type shoulder, where there is a deeper saddle for the H_2 + CO_2 case but less so for the H_2 only case, indicating a small O_{vac} fraction decrease from 22% in the H_2 -only condition to 18% in H_2 + CO_2 photoillumination. Taken together, it is clear that the presence of OH and O_{vac} sites create a strong polarization effect in both homolytic and heterolytic dissociation of H_2 to form hydride H^- adatoms on the neighboring indium sites, H^+OH sites, and H^+O sites. The O1s spectra consistently shows a high OH-type peak with an increased binding energy compared to vacuum conditions. H^+OH and H^+O sites, thus, persist mostly under photoillumination conditions due to stabilizing effects of the addition of photoexcited holes. In addition, there is also some indication that oxygen vacancies are filled in the CO_2 -only and H_2 + CO_2 atmosphere. A possible reaction pathway involves carbonate filling of oxygen vacancies to form a bidentate-like carbonate with a C–O bond, with an adsorption

energy of -0.61 eV. This is activated by a neighboring In–H hydride to form a formate species, with a small activation energy barrier of 0.15 eV and an exothermic reaction energy of -0.21 eV [12].

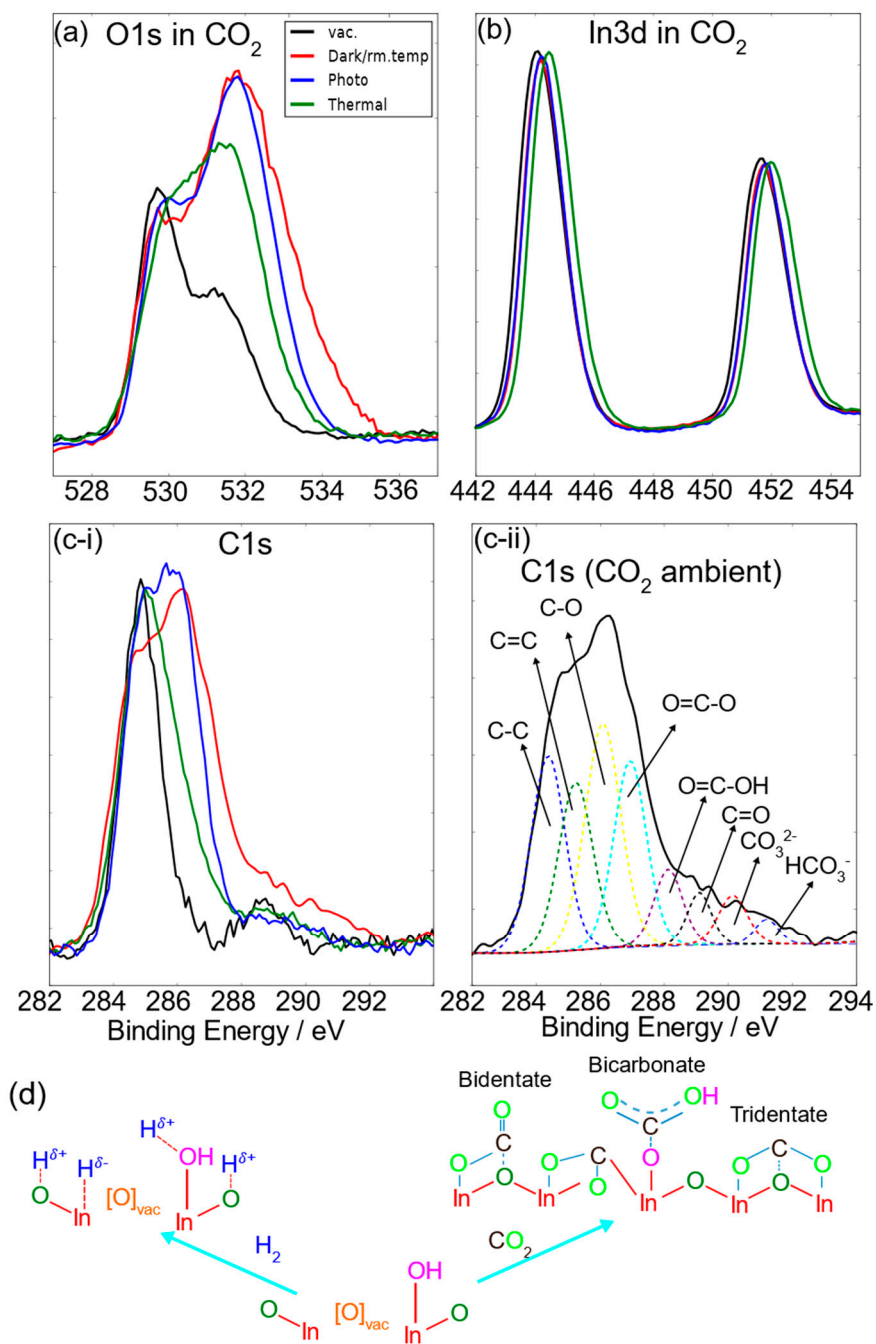


Figure 3. (a–c) The O1s, In3d, and C1s XPS spectra of $\text{In}_2\text{O}_{3-x}(\text{OH})_y$ nanorods in CO_2 under various reactor conditions in comparison with the pristine surface shown in Figure 1. (d) The two adsorption pathways for a defective $\text{In}_2\text{O}_{3-x}(\text{OH})_y$ surface for H_2 - and CO_2 -only atmospheres. For bidentate configurations, the adsorption energy was determined [12] to be -0.70 eV; tridentate had -1.25 eV adsorption energy; and CO_2 adsorbed on an oxygen vacancy with an adsorption energy of -0.61 eV.

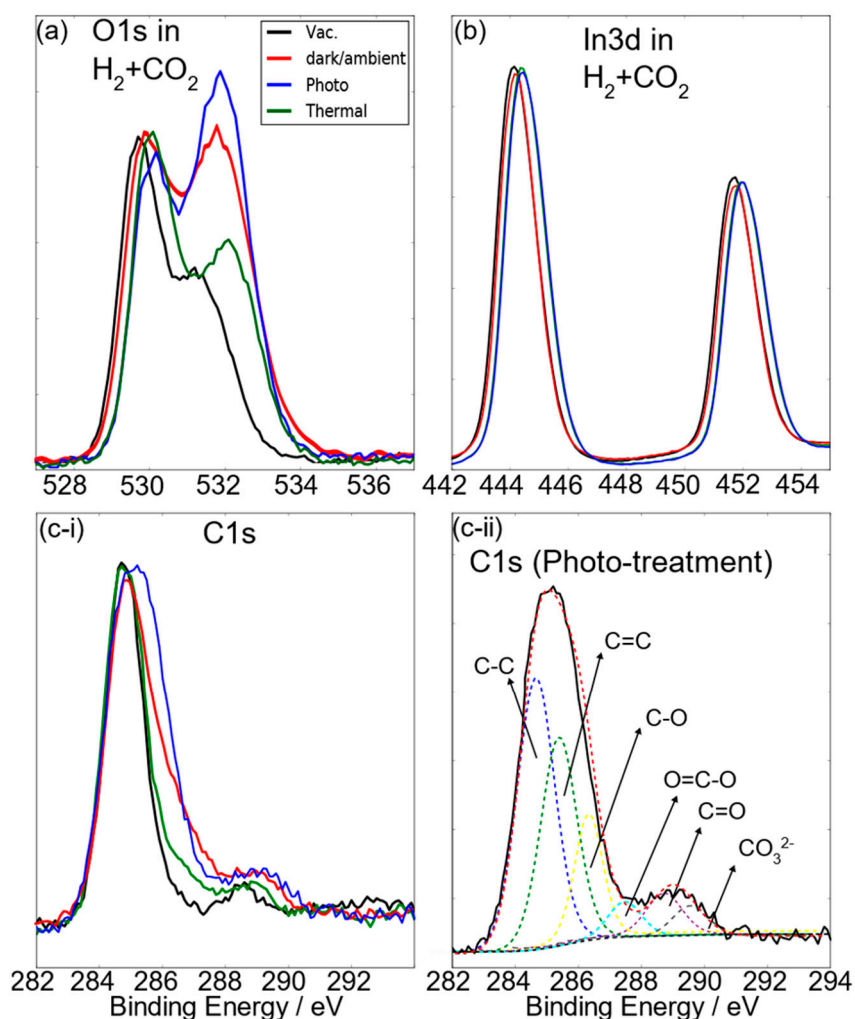


Figure 4. (a–c) The O1s, In3d, and C1s XPS spectrum of $\text{In}_2\text{O}_{(3-x)}(\text{OH})_y$ nanorods in H_2+CO_2 under various reactor conditions in comparison with the pristine surface shown in Figure 1. (c-ii) shows the various carbon species in the C1s spectrum after H_2+CO_2 under photoillumination conditions.

We now turn to in situ Hall measurements to examine the surface reactivity in greater depth (Figure 5). Generally, electrical resistivity (Figure 5a) decreases with photoillumination, with the greatest decrease occurring in vacuum atmosphere with H_2 , followed by H_2+CO_2 , and the smallest decrease occurring in vacuum atmosphere for CO_2 . CO_2 and CO_2+H_2 show the smallest photoinduced resistivity decrease of $\sim 10\%$ and $\sim 13\%$, respectively. For the associated carrier concentration trends, carrier concentrations also follow the trends of the resistivity plot for vacuum and CO_2 , however, for H_2+CO_2 , there is a distinct difference in the temperature dependence slope, with the slope under photoillumination being greater than that of the dark condition. Furthermore, the carrier concentration for H_2 dark and photoilluminated conditions are relatively similar in the same order of magnitude, with a steeper temperature dependence under photoillumination than under dark conditions. Generally, carrier mobility decreases under photoillumination, with increased electron–hole pair recombination as a result of carrier concentration increase; hence, there is also a logarithmic linear dependence between mobility and concentration, as shown in Figure 5c. $\text{In}_2\text{O}_{(3-x)}(\text{OH})_y$ in CO_2 atmosphere has generally low carrier concentrations and lower intrinsic carrier mobilities (extrapolated mobilities at very low concentrations) because of higher electron–hole pair recombination rates. Interestingly, the intrinsic carrier mobilities in vacuum are higher than in the H_2 or CO_2 atmospheres, showing that reactant gas chemisorption induces higher recombination rates. The H_2+CO_2 atmosphere mobility concentration trend is, however, very similar to that of the vacuum trend.

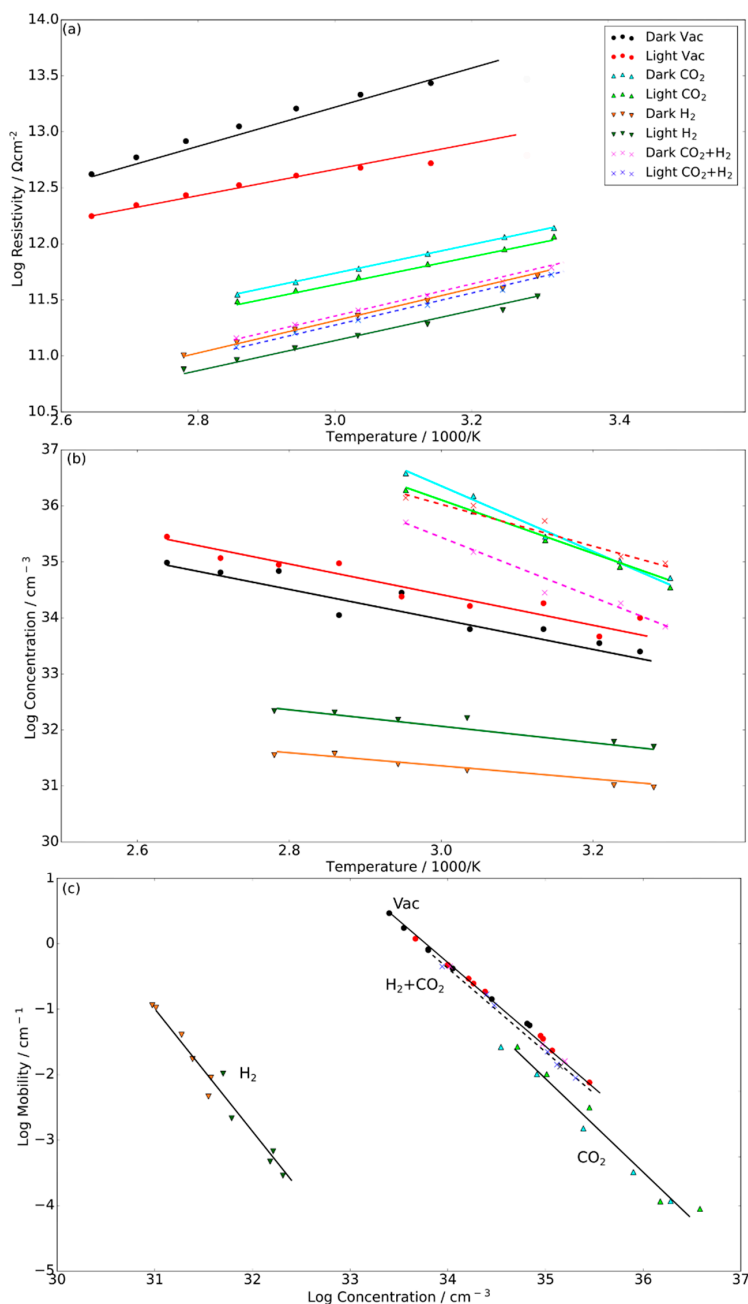


Figure 5. (a) Electrical resistivity and (b) carrier concentration as a function of temperature, with (c) carrier mobility and concentration trends. The results for the vacuum, H_2 , CO_2 , and H_2+CO_2 atmospheres are indicated with circle, downside triangle, upside triangle, and cross markers, respectively. Trend lines are shown as a visual guide, with dotted lines representing CO_2+H_2 atmospheres.

The trends shown in Hall measurements can be mostly explained by the aforementioned XPS results. A majority homolytic dissociation of H_2 injects free electrons through $\frac{1}{2}\text{H} + \text{O}_L \rightarrow \text{OH}^+ + e^-$ and $\text{OH} + \frac{1}{2}\text{H}_2 \rightarrow \text{H}^+\text{OH} + e^-$, whereas heterolytic dissociation of H_2 to form indium hydride generates hole states that can be recombined with any electrons generated from homolytic dissociation. This would explain the sharper increase of carrier concentrations from dark ambient temperature to dark high temperatures, as well as the larger spread of the concentration–mobility trend in comparison to other gas atmospheres. Since the homolytic dissociation of H_2 under photo condition is fairly similar to that of the 150°C thermal condition, photoillumination and thermal conditions would likely induce greater homolytic dissociation of H_2 , which can be rationalized in the intersecting trend

of increasing carrier concentration with increasing temperature under photo and dark conditions. The increase in carrier concentration as a result of H_2 dissociation is, however, partly mitigated by the decrease in carrier mobilities, since H^+OH groups can act as strong electron traps. The trends shown with the CO_2 -only atmosphere indicate that carbonate adsorption depletes free carrier densities and that surface carbonates act as significant carrier scattering sites that increase recombination rates. Since phototreatment induces less carbonate formation, the depletion of free carrier density is reduced, leading to an increase in free carrier density. Furthermore, carbonate formation decreases with temperature, which can explain the increase in concentration with temperature; however, because carbonates are still seen at high temperatures, the increase in carrier density is more gradual. Under H_2+CO_2 , the mixture of H_2 dissociation and carbonate formation results in a dynamic carrier population that has both the characteristics of CO_2 - and H_2 -only trends. In dark thermal conditions, homolytic dissociation on the OH group is shown to be more likely than on oxygen lattice sites. As such, the more gradual concentration increase than for H_2 -only group can be linked to lower dissociation of H_2 . In photoillumination condition, while the OH shoulder expansion may indicate either prevalent H_2 dissociation or prevalent carbonate absorption, the higher carrier concentration compared to that of dark condition indicates that H_2 dissociation is more favored than carbonate absorption. However, the gradual sloping of the temperature dependence in photoillumination may indicate that carbonate absorption is slightly more favored at higher temperatures under photoillumination.

3. Conclusions

In conclusion, quasi-operando XPS and in situ Hall measurements with the various reactant atmospheres and reactor parameters have provided a new window into the reaction of gaseous H_2 , CO_2 , and H_2+CO_2 with nanostructured $In_2O_{(3-x)}(OH)_y$ under photochemical and thermochemical operating conditions. While changes in the O1s and In3d core level ionization potentials clearly depict the dissociative adsorption of H_2 on the surface of nanostructured $In_2O_{(3-x)}(OH)_y$, the results clearly distinguish the homolysis from the heterolysis pathway. These results also show the importance of photoillumination and the reason for $In_2O_{(3-x)}(OH)_y$ as being a high efficacy photocatalyst, which is to induce greater H_2 dissociation and carbonate stability than under thermal conditions. The Hall results show the link between the surface compositional changes with electronic activity, with varying temperature and photo-dependences due to the various populations of chemisorbed species. These results show that surface compositions play important roles in the multiple step process of the RWGS, and can be utilized for various photocatalysts and carbon-based nanocomposites [22–24].

4. Materials and Methods

Synthesis Procedure: The $In_2O_{(3-x)}(OH)_y$ nanorod structures discussed in this paper were fabricated through the following steps: 0.397 g of $InCl_3$ was dissolved in 6ml ethanol with stirring. A separate mixture of 2.5 mL NH_3OH , 7.5 mL ethanol, and 2 mL H_2O was mixed in the $InCl_3$, creating a white suspension. To control for uniform size distributions, the white suspension was immersed in a heated oil bath at 80 °C with stirring for 10 min. The suspension was then centrifuged, excess solvent was removed, and it was subsequently washed with deionized water. This step was done 3 times before a vacuum drying procedure at 70 °C for 12 h. The dried powder was then calcined for 12 h at 250 °C to form the $In_2O_{(3-x)}(OH)_y$ phase nanorod structures. The nanorods had an average length of 1800 nm, 13 nm diameter, and Brunauer-Emmett-Teller (BET) derived surface area of 151 m^2/g .

XPS measurements: The reactor-based quasi-operando XPS measurements were performed with the intention of mimicking the reactor sequence in reducing CO_2 with H_2 with this material system. The powder samples were placed on glass slides and a glass pipette, which were used to roll and drag the powders until a visibly smooth film was obtained. Three samples were prepared for each gas condition (H_2 , CO_2 , and H_2+CO_2). Each sample was placed in a high vacuum ConFlat flange assembly and sealed with a UV-enhanced transmissive viewport flange using copper gaskets. H_2 and CO_2 were introduced at 2 atm pressure after vacuum pumping to $\sim 2 \times 10^{-5}$ mbar. For H_2+CO_2 , H_2 was

introduced at 2 atm pressure, vented to 1 atm pressure, and CO₂ was introduced at 1.6 atm pressure. The reactors were then subjected to phototreatment (40 W/cm² intensity white lamp), thermal treatment (150 °C), or control condition (no photoillumination and no thermal treatment) for ~12 h. The nanorod samples were then removed from their reactors inside a grade 5 argon-filled glovebox with O₂ and H₂O concentrations of 0.5–0.7 ppm and 0.1–0.3 ppm, respectively. They were then attached to the XPS instrument and loaded directly into the instrument. The instrument was an Thermo Scientific™ ESCALAB™ XPS system (Thermo Scientific, Waltham, MA, USA).

Hall measurements: The in situ hall measurements were carried out on a modified Nanometrics Hall system, where the sample box was sealed after applying the contact probes on the sample, which had 4 square gold electrodes 2 mm in width and 500 nm thickness at the corners of the sample film. The electrodes were set 0.5 mm apart. After sealing the sample box, a rough vacuum pumping was applied, after which the gas atmospheres were introduced with a 1.3 atmosphere pressure, and a pressure release valve equilibrated the pressure to 1 atmosphere pressure.

Supplementary Materials: The following are available online. Figure S1. XPS deconvolution after H₂ immersion. While the Ovac specie remain relatively constant, the OHT group increase by 144% is significant in H₂ dark ambient. 26–28% of OHB group is lost in photo/ thermal condition. Figure S2. XPS deconvolution after CO₂ immersion. Control means dark ambient temperature conditions. For photo condition, there is a significant C–O and O=C–O peak whereas in thermal condition C–O peak increases. Figure S3. XPS O1s deconvolution after H₂ + CO₂ immersion. Under dark ambient and photo condition, the OH shoulder expands to nearly 50% of the total O type species. Figure S4. Left figure. C13 CO₂ isotope testing by GCMS Agilent 5975C with Mass Spectrometry. The C13O peak is identified at the 1.33 min mark. Right figure, EPR of nanorod powder in quartz capillary tube. To fit the spectrum, the g factors of 3 spin systems with isotropic states are 2.04; 2.116; 2.18 with spin concentration ratios of 0.35:1:0.1 respectively. Figure S5. The UV-Vis spectrum of the In₂O_{3-x}(OH)_y powder film, showing the weak absorption tail in the visible which can be associated with band gap deep defects.

Author Contributions: Conceptualization, J.Y.Y.L.; Methodology, J.Y.Y.L.; Software, J.Y.Y.L.; Validation, J.Y.Y.L.; Resources, N.P.K.; Data Curation, J.Y.Y.L.; Writing-Original Draft Preparation, J.Y.Y.L.; Writing-Review & Editing, J.Y.Y.L., N.P.K.; Visualization, J.Y.Y.L.; Supervision, N.P.K.; Funding Acquisition, N.P.K.

Funding: This research received no external/corporate funding.

Acknowledgments: The authors gratefully acknowledge funding from the Natural Sciences and Engineering Research Council of Canada (NSERC), the Canadian Foundation for Innovation (CFI), and the Ontario Research Fund. The authors also acknowledge the kind assistance of L. He in the preparation of the nanorods, as well as the discussions with Professor G. Ozin and others.

Conflicts of Interest: The authors declare no conflict of interest.

References

1. Liu, S.; Tang, Z.-R.; Sun, Y.; Colmenares, J.C.; Xu, Y.-J. One-dimension-based spatially ordered architectures for solar energy conversion. *Chem. Soc. Rev.* **2015**, *44*, 5053–5075. [[CrossRef](#)]
2. Yuan, L.; Xu, Y.-J. Photocatalytic conversion of CO₂ into value-added and renewable fuels. *Appl. Surf. Sci.* **2015**, *342*, 154–167. [[CrossRef](#)]
3. Ma, Y.; Wang, X.; Jia, Y.; Chen, X.; Han, H.; Li, C. Titanium Dioxide-Based Nanomaterials for Photocatalytic Fuel Generations. *Chem. Rev.* **2014**, *114*, 9987–10043. [[CrossRef](#)] [[PubMed](#)]
4. Hoch, L.B.; Wood, T.E.; O'Brien, P.G.; Liao, K.; Reyes, L.M.; Mims, C.A.; Ozin, G.A. The rational design of a single component photocatalyst for Gas Phase CO₂ reduction using both UV and Visible Light. *Adv. Sci.* **2014**, *1*, 1400013. [[CrossRef](#)] [[PubMed](#)]
5. Wang, L.; Ghossoub, M.; Wang, H.; Shao, Y.; Sun, W.; Tountas, A.A.; Wood, T.E.; Li, H.; Loh, J.Y.Y.; Dong, Y.; et al. Photocatalytic Hydrogenation of Carbon Dioxide with High Selectivity to Methanol at Atmospheric Pressure. *Joule* **2018**, *2*, 1369–1381. [[CrossRef](#)]
6. Martin, O.; Martín, A.J.; Mondelli, C.; Mitchell, S.; Segawa, T.F.; Hauert, R.; Drouilly, C.; Curulla-Ferré, D.; Pérez-Ramírez, J.; Curulla-Ferré, D.; et al. Indium Oxide as a Superior Catalyst for Methanol Synthesis by CO₂ Hydrogenation. *Angew. Chem. Int. Ed.* **2016**, *55*, 6261–6265. [[CrossRef](#)]
7. Dong, Y.C. Tailoring surface Frustrated Lewis Pairs of In₂O_(3-x)OH_y for gas phase Heterogeneous photocatalytic reduction of CO₂ by isomorphous substitution of In³⁺ with Bi³⁺. *Adv. Sci.* **2018**, *5*, 1700732. [[CrossRef](#)]

8. He, L.; Wood, T.E.; Wu, B.; Dong, Y.; Hoch, L.B.; Reyes, L.M.; Wang, D.; Kubel, C.; Qian, C.; Jia, J.; et al. Spatial Separation of charge carriers in $\text{In}_2\text{O}_{(3-x)}(\text{OH})_y$ Nanocrystal superstructures for enhanced gas-phase photocatalytic activity. *ACS Nano* **2016**, *10*, 5578–5586. [[CrossRef](#)]
9. Stephan, W.D. Frustrated Lewis Pairs. *J. Am. Chem. Soc.* **2015**, *137*, 10018–10032. [[CrossRef](#)]
10. Ghuman, K.K.; Hoch, L.B.; Szymanski, P.; Loh, J.Y.Y.; Kherani, N.P.; El-Sayed, M.A.; Ozin, G.A.; Singh, C.V. Photoexcited Surface Frustrated Lewis Pairs for Heterogeneous Photocatalytic CO_2 Reduction. *J. Am. Chem. Soc.* **2016**, *138*, 1206–1214. [[CrossRef](#)]
11. Taifan, W.; Boily, J.-F.; Baltrusaitis, J. Surface chemistry of carbon dioxide revisited. *Surf. Sci. Rep.* **2016**, *71*, 595–671. [[CrossRef](#)]
12. Ye, J.; Liu, C.-J.; Ge, Q. DFT Study of CO_2 Adsorption and Hydrogenation on the In_2O_3 Surface. *J. Phys. Chem. C* **2012**, *116*, 7817–7825. [[CrossRef](#)]
13. Ghuman, K.K.; Hoch, L.B.; Wood, T.E.; Mims, C.; Singh, C.V.; Ozin, G.A. Surface Analogues of Molecular Frustrated Lewis Pairs in Heterogeneous CO_2 Hydrogenation Catalysis. *ACS Catal.* **2016**, *6*, 5764–5770. [[CrossRef](#)]
14. Ghuman, K.K.; Hoch, L.B.; Mims, C.A.; Wood, T.E.; Ozin, G.A.; Singh, C.V. Illuminating CO_2 reduction on frustrated Lewis pair surfaces: Investigating the role of surface hydroxides and oxygen vacancies on nanocrystalline $\text{In}_2\text{O}_{(3-x)}(\text{OH})_y$. *Phys. Chem. Chem. Phys.* **2015**, *17*, 14623–14635. [[CrossRef](#)] [[PubMed](#)]
15. Chen, H.-Y.T.; Giordano, L.; Pacchioni, G. From Heterolytic to Homolytic H_2 Dissociation on Nanostructured MgO (001) Films as a Function of the Metal Support. *J. Phys. Chem. C* **2013**, *117*, 10623–10629. [[CrossRef](#)]
16. Scarano, D.; Bertarione, S.; Cesano, F.; Vitillo, J.G.; Zecchina, A. Plate-like zinc oxide microcrystals: Synthesis and characterization of a material active toward hydrogen adsorption. *Catal. Today* **2006**, *116*, 433–438. [[CrossRef](#)]
17. García-Melchor, M.; Homolytic, N.L. Products from Heterolytic Paths in H_2 Dissociation on Metal Oxides: The Example of CeO_2 . *Phys. Chem. C* **2014**, *118*, 10921–10926. [[CrossRef](#)]
18. Yang, J.; Cheng, H.; Martens, W.N.; Frost, R.L. Application of Infrared emission spectroscopy to the thermal transition of indium hydroxide to indium oxide nanocubes. *Appl. Spectrosc.* **2011**, *65*, 113–118. [[CrossRef](#)]
19. Wagner, M.; Lackner, P.; Seiler, S.; Brunsch, A.; Bliem, R.; Gerhold, S.; Wang, Z.; Osiecki, J.; Schulte, K.; Boatner, L.A.; et al. Resolving the Structure of a Well-Ordered Hydroxyl Overlayer on $\text{In}_2\text{O}_3(111)$: Nanomanipulation and Theory. *ACS Nano* **2017**, *11*, 11531–11541. [[CrossRef](#)]
20. Loh, J.Y.; Kherani, N.P. In Situ Electronic Probing of Photoconductive Trap States for the Catalytic Reduction of CO_2 by $\text{In}_2\text{O}_{(3-x)}(\text{OH})_y$ Nanorods. *J. Phys. Chem. Lett.* **2019**, *10*, 526–532. [[CrossRef](#)]
21. Gan, J.; Lu, X.; Wu, J.; Xie, S.; Zhai, T.; Yu, M.; Zhang, Z.; Mao, Y.; Wang, S.C.I.; Shen, Y.; et al. Oxygen vacancies promoting photoelectrochemical performance of In_2O_3 nanocubes. *Sci. Rep.* **2013**, *3*, 3. [[CrossRef](#)] [[PubMed](#)]
22. Khan, M.E.; Cho, M.H. Green synthesis, photocatalytic and photoelectrochemical performance of an Au—Graphene nanocomposite. *RSC Adv.* **2015**, *5*, 26897–26904. [[CrossRef](#)]
23. Mohammad, A.; Khan, M.E.; Karim, M.R.; Cho, M.H. Synergistically effective and highly visible light responsive SnO_2 -g- C_3N_4 nanostructures for improved photocatalytic and photoelectrochemical performance. *Appl. Surf. Sci.* **2019**, *495*, 143432. [[CrossRef](#)]
24. Mohammad, A.; Karim, M.R.; Khan, M.E.; Khan, M.M.; Cho, M.H. Biofilm-Assisted Fabrication of Ag@SnO_2 -g- C_3N_4 Nanostructures for Visible Light-Induced Photocatalysis and Photoelectrochemical Performance. *J. Phys. Chem. C* **2019**, *123*, 20936–20948. [[CrossRef](#)]

Sample Availability: Samples of the compounds are available from the authors.



© 2019 by the authors. Licensee MDPI, Basel, Switzerland. This article is an open access article distributed under the terms and conditions of the Creative Commons Attribution (CC BY) license (<http://creativecommons.org/licenses/by/4.0/>).